ADVANCED OPTICAL MATERIALS
www.advopticalmat.de

Ultrabroadband Excitation of Hot Carriers in Plasmonic Nanorods Revealed by Two-Dimensional Electronic Spectroscopy

*Andrea Schirato, Mattia Russo, Luca Moretti, Alessandro Molinelli, Laura Polito, Filippo Rossi, Giulio Cerullo, Giuseppe Della Valle, and Margherita Maiuri**

Plasmonic nanostructures photoexcited with ultrashort light pulses exhibit a strong nonlinear optical response driven by nonequilibrium 'hot' carriers. Studying the spectro-temporal evolution of such nonlinearities to extract information on hot electron dynamics has attracted significant interest, given the unparalleled opportunities unlocked by these high-energy carriers in fields ranging from photocatalysis to optical communications. However, in typical samples of size-dispersed nanoparticles, effects such as inhomogeneous broadening and pump-pulse-induced selectivity can distort the system response, hindering accurate characterizations. This study dissects the ultrafast response of polydisperse gold nanorods employing two-dimensional electronic spectroscopy (2DES), a powerful technique offering a unique combination of temporal and spectral resolution. The ultrabroadband pulses cover both the transverse and longitudinal nanorod resonances, enabling an accurate analysis of their distinct behavior. By complementing experiments with a quantitative model of hot-carrier-mediated nonlinearities that incorporates sample polydispersity, the broadband excitation, and the nanorods' resonant absorption, the work provides a comprehensive understanding of the underlying mechanisms and identifies fingerprints of electron–electron scattering in the 2DES maps. Performed on a simple yet prototypical system, this analysis advances the study of plasmonic hot carriers and supports further applications of 2DES to explore ultrafast mechanisms in more advanced hybrid plasmon-based systems, e.g. strongly-coupled complexes.

1. Introduction

Metallic nanostructures have established themselves as a robust platform for enhancing, probing, and manipulating light-matter interactions at the nanoscale,[1,2] enabling a broad spectrum of applications ranging from photodetection to biochemical sensing.[3–5] Their unique role in fields as diverse as light-energy conversion and ultrafast nanophotonics originates from the distinctive optical response of plasmonic nano-systems.

In essence, photon absorption can resonantly excite a collective coherent oscillation of free charges in the metal, known as a localized surface plasmon (LSP), which confines electromagnetic fields within nanometric volumes.[6] Upon dephasing (within ≈10 fs), the LSP decays non-radiatively, resulting in the generation of 'hot' carriers, i.e., electron-hole pairs with very high energies (up to a few eV) and ultrashort lifetime (femto- to picosecond timescale).[7–9] Specifically, relaxation of these nonequilibrium carriers is dictated by internal electron–electron

---

A. Schirato, M. Russo, L. Moretti, G. Cerullo, G. Della Valle, M. Maiuri
Dipartimento di Fisica
Politecnico di Milano
P.zza Leonardo da Vinci 32, Milan 20133, Italy
E-mail: margherita.maiuri@polimi.it

A. Schirato
Department of Physics and Astronomy
Rice University
6100 Main Street, Houston, TX 77005, USA

G. Cerullo
Istituto di Fotonica e Nanotecnologie – Consiglio Nazionale delle Ricerche
P.zza L. da Vinci, 32, Milano 20133, Italy

A. Molinelli, F. Rossi
Dipartimento di Chimica, Materiali Ingegneria Chimica "Giulio Natta"
Politecnico di Milano
via Mancinelli 7, Milan 20131, Italy

L. Polito
Consiglio Nazionale delle Ricerche
CNR-SCITEC
Via G. Fantoli 16/15, Milan 20138, Italy

The ORCID identification number(s) for the author(s) of this article can be found under https://doi.org/10.1002/adom.202503283

DOI: 10.1002/adom.202503283

thermalization (hundreds of fs), and energy dissipation through electron-phonon coupling (within tens of ps), followed by a slower heat exchange between the lattice and the environment.[10]

Effectively harnessing the large excess energy of plasmonic hot carriers before their return to equilibrium offers an exceptional opportunity for accessing and controlling a wealth of photoinduced phenomena.[11] For instance, nonlinear optical processes have been successfully modulated at ultrahigh speed by all-optical means.[12,13] Likewise, in various hybrid systems, where metallic nanostructures are coupled, e.g., to molecular complexes or semiconductors (at the nanoscale and below, using transition metal dichalcogenides), hot carrier injection and energy transfer have been exploited for photocatalysis and energy conversion.[14–17]

Given their vast potential, plasmonic hot carriers and their ultrafast dynamics have been the focus of extensive research.[18–21] Time-resolved optical techniques have proven to be an invaluable tool to probe how photoexcited electronic states alter the optical response of metallic nanostructures. Indeed, the nonequilibrium energy distribution of these carriers induces strong Kerr-like nonlinear modifications of the metal's optical properties,[22–24] which can be monitored with ultrashort probe pulses. Specifically, transient absorption (TA) spectroscopy[25] has significantly advanced our understanding of ultrafast hot-carrier dynamics, revealing how factors such as configuration, geometry, and composition impact their evolution and spectral signatures across various systems.[26–31]

However, the spectro-temporal features of typical TA signals measured on ensembles of nanostructures are often affected by inhomogeneous broadening, due to shape and size dispersion. While this effect can be mitigated in ordered systems, such as metasurfaces (i.e., planar ordered arrangements of nanoantennas), where lithographic fabrication techniques ensure uniformity, colloidal solutions are commonly polydisperse, exhibiting significant inhomogeneities. This broadening can pose a challenge when analyzing resonant optical modes that are sensitive to the nanoparticle shape and size.

The simplest and most prototypical plasmonic system illustrating such a situation is an ensemble of nanorods (NRs), which support: (i) a transverse LSP (Tr-LSP), quasi-static in nature, and thus inherently less sensitive to size variations; and (ii) a longitudinal LSP (Lg-LSP), whose spectral position is strongly dependent on the NR aspect ratio. In such ensemble, shape dispersion can distort or average out the transient effects driven by hot carriers in the Lg-LSP spectral region, hindering the precise characterization of the electrons' dynamics and the resonant mode's evolution. Additionally, the inhomogeneous broadening of the absorption spectrum introduced by even slight variations in NR size leads to the selective excitation of NR subsets when using quasi-monochromatic pump pulses,[32–34] which can further alter or skew the dynamics of the entire system. More broadly, similar issues arise for complex, possibly multimodal nanoparticle morphologies and configurations.

A promising strategy to overcome these limitations is offered by two-dimensional electronic spectroscopy (2DES).[35] This technique is an extension of broadband TA in which a second pump pulse is added, and the time delay between the first two pump pulses is controlled with interferometric precision, allowing one to obtain energy resolution across the pump spectrum through Fourier transform spectroscopy.[36] The result is a correlation map between the pump ('excitation') and probe ('detection') frequencies for each pump–probe delay (defined as 'population' time). Combining high spectral and temporal resolution exceeding the capabilities of conventional TA spectroscopy, 2DES has become the method of choice for dissecting correlations between excitation and detection frequencies, identifying coherences and couplings between states, and resolving highly congested energy landscapes.[37,38] In recent years, 2DES has proven uniquely incisive in investigating energy transfer, vibronic coupling, and quantum coherence, and it has been extensively applied to molecular systems,[39–41] light-harvesting complexes,[42,43] and thin semiconductors.[44,45] Yet, despite its potential, only a few studies have applied 2DES to the investigation of plasmonic nanostructures.[46–51] 2DES not only addresses the challenges posed by inhomogeneous broadening and spectral selectivity, but, with its exclusive capability to unfold the excitation-frequency axis and correlate excitation and detection frequencies over time, it also holds promise for elucidating energy-dependent mechanisms such as the photogeneration and energy transfer of hot carriers. It thus promises to offer new fundamental insights which could guide the design of engineered hybrid systems e.g. for photocatalytic applications.[52]

In this study, we utilized 2DES to investigate the ultrafast nonlinear response of colloidal Au NRs. We employed ultrashort (< 15 fs) pulses with an ultrabroadband spectrum spanning 1.71–2.47 eV (500–720 nm), concurrently covering both the transverse and longitudinal plasmonic modes of the NRs. This allowed us to probe simultaneously their excitation, and analyse their distinct nonequilibrium behaviors in the presence of size dispersion, a significant advancement over prior studies, which were restricted to interrogating either a single mode,[46,47,51] or both modes, albeit spectrally overlapping.[48] To gain deeper insights into the system's response to the broadband ultrafast excitation, 2DES measurements were complemented with quantitative numerical modelling of the transient optical nonlinearities mediated by hot carriers. An original approach was developed, building upon and extending previously established models, to consistently incorporate the broadband character of the excitation, the spectral dispersion of the NRs absorption, and the size dispersion inherent to the experimental sample.

By presenting a simple yet representative system, our analysis on Au NRs introduces a comprehensive approach to probe the hot-electrons dynamics even in disordered plasmonic nanostructures, and paves the way for applying 2DES to more complex hybrid systems[49,50,53] with tailored electronic properties.

2. Results and Discussion

The aqueous solution of colloidal Au NRs was prepared following the synthetic procedure described in the Experimental Section under heading "Sample Preparation". The resulting NRs were relatively isolated, with regular shapes and uniform morphological properties, as evidenced by representative TEM images of the solution (shown as insets in **Figure** 1b). For a quantitative dimensional analysis of the NRs, TEM images at lower magnifications were acquired and analyzed (see Figure S1 and Section S1, Supporting Information) to characterise the particle size dispersion within the sample. By examining ≈680 NRs in a correlated

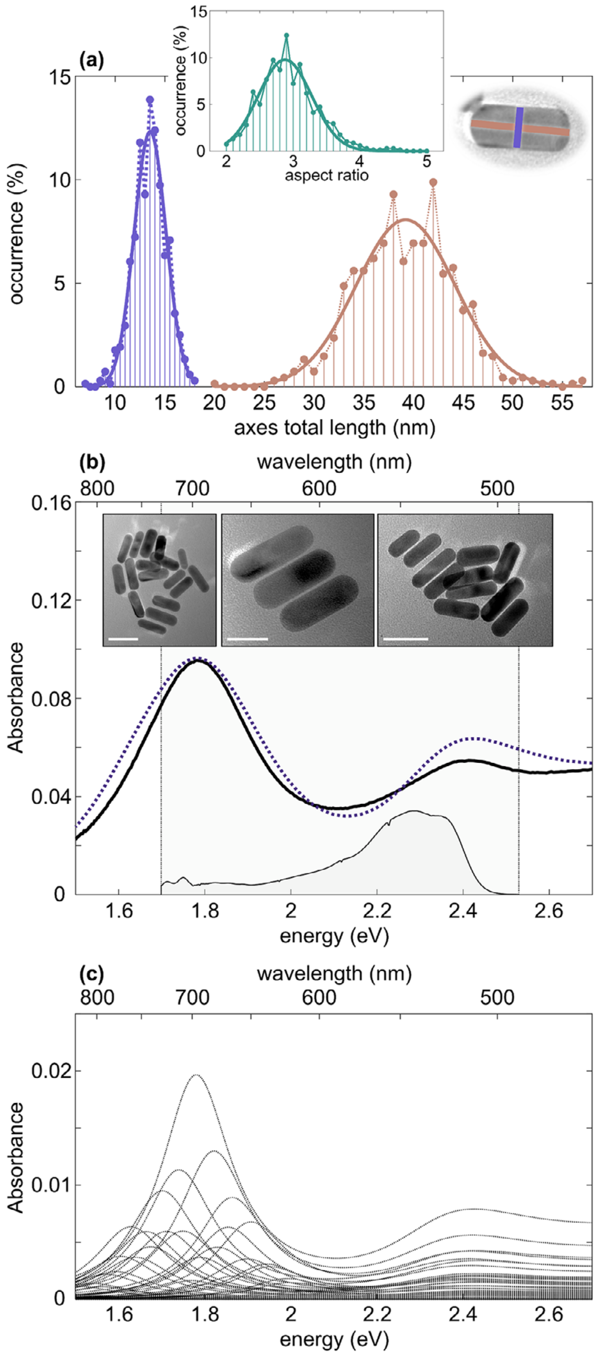

Figure 1. Plasmonic NRs static response. a) Size distribution of the widths (purple) and lengths (brown) of our NRs extracted from the correlated analysis of a TEM image. The top inset shows the size distribution of the corresponding AR. Solid lines are Gaussian fits of the measured distribution. b) Experimental (black solid) and simulated (blue dotted) static absorbance of the sample. The (normalized) power spectral density $S_p(h\nu)$ of the pulses used in the ultrafast measurements is also shown (gray area), and the spectral region where it overlaps with the sample absorbance is highlighted (gray shade). The top insets show three exemplary TEM images of the colloidal NRs in solution (aqueous environment). Scale bars are, from left to right, 40, 20, and 40 nm, respectively. c) Simulated absorbance spectra of all the mono-disperse subsets considered in the numerical model (100 in total), weighted over the relative occurrence estimated from TEM analysis.

fashion, we obtained the distributions of lengths, widths, and aspect ratios (ARs), shown in Figure 1a alongside a Gaussian fit of the data.

The extracted NR average length was 39.2 ± 5 nm, width 13.5 ± 1.6 nm, and AR 2.8 ± 0.4, indicating a size variability that affects the static optical response of the ensemble in distinct ways. Indeed, it is well known that the rod width and length govern the resonant excitation of its transverse (Tr) and longitudinal (Lg) LSPs, respectively, and that these modes respond differently to size variations. The Tr-LSP is a quasi-static mode, hence it is almost insensitive to changes in width. On the contrary, the Lg-LSP is strongly affected (both in amplitude and spectral position) by the NR length (or, equivalently, its AR). As a result, the NRs length distribution contributes significantly to the inhomogeneous broadening of the Lg-LSP resonance in the ensemble, whereas the Tr-LSP is expected to remain primarily governed by homogeneous broadening.

To characterise the optical behavior of the sample, we measured its static absorbance Abs($h\nu$), shown in Figure 1b (solid black curve). The spectrum exhibits two well-defined resonant peaks at 1.78 eV (695 nm) and 2.41 eV (515 nm), assigned to the Lg- and Tr-LSP modes of the NRs, respectively. Their significant spectral separation (>600 meV), consistent with the relatively large average AR and in agreement with previous reports,[54] is a key aspect of our investigation. This separation allowed us to track the spectro-temporal features of the two modes in the ultrafast regime with minimal spectral overlap.

The static measurement was complemented by a numerical model, which predicts an absorbance spectrum in excellent agreement with the experiment (compare dotted blue and solid black lines in Figure 1b). For an accurate description of the sample, the model incorporates its polydispersity, using the size distributions retrieved from the TEM dimensional analysis. Specifically, the NRs were grouped by size into subsets, each identified by a specific width, length, and relative occurrence. Treating each subset as monodisperse at a given NR concentration (set to 80% of the experimental value for the best quantitative match), we applied analytical calculations[55] to determine their absorbance. Further details can be found in the Experimental Section under heading “Numerical Modelling”. Figure 1c shows the simulated spectra for all subsets considered in the model, with their amplitude weighted by their relative occurrence. The weighted sum of these spectra yields the absorbance of the overall polydisperse sample shown in Figure 1b (blue dotted curve). Note that, by retaining information on the optical response of individual subsets, our model accounts for the distinct broadening mechanisms of the Tr- and Lg-LSPs, as evidenced in Figure 1c. While all simulated subsets exhibit the Tr-LSP at nearly the same energy, their Lg-LSP modes show significant variability, leading to the inhomogeneous broadening of the peak observed in both the total simulated and measured absorbance.

To study the ultrafast optical response of the sample, we performed 2DES experiments. This technique (detailed in the Experimental Section under heading “Two-Dimensional Electronic Spectroscopy Experiments”, see also Figure S2 and Section S2, Supporting Information) allowed us to track the photoinduced nonequilibrium dynamics of the NR ensemble with 15-fs temporal resolution, while also providing high excitation photon energy resolution. The experimental ultrabroadband power spectral

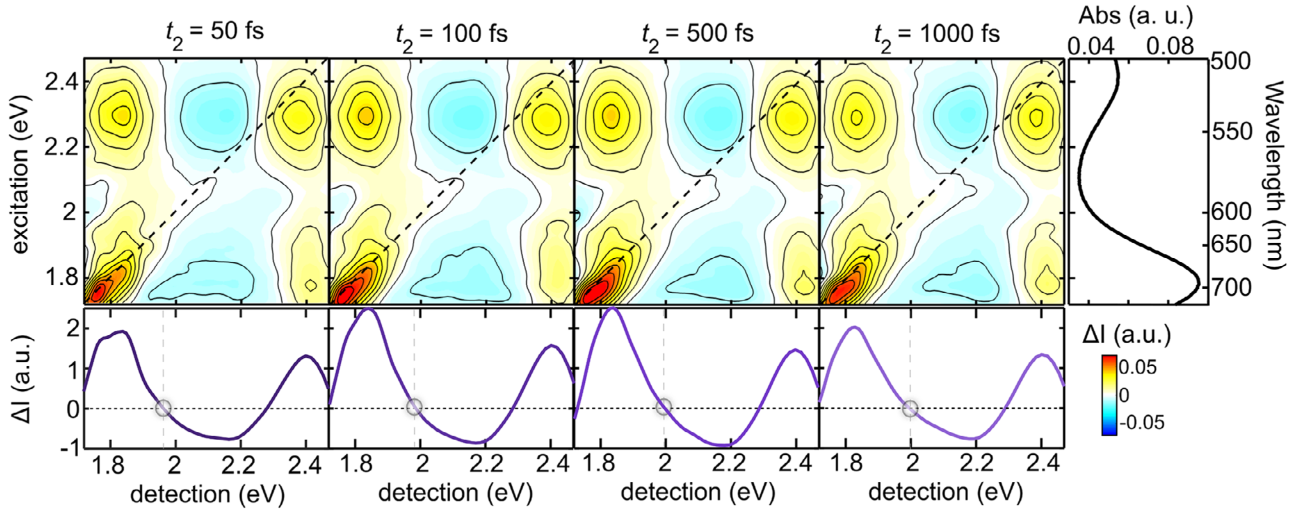

Figure 2. Two-dimensional electronic spectroscopy on plasmonic NRs. Purely absorptive 2DES maps of the Au NRs in solution at $t_2 = 50$ fs, 100 fs, 500 fs, and 1 ps, from left to right, respectively. The 2DES signal integrated over the excitation energy axis is reported in the bottom panels for each t_2 delay. The grey circles identify the low-energy isosbestic point of the spectra. The measured static absorption is also shown on the rightmost side of the 2DES maps.

density $S_p(h\nu)$ of the pulses, reported in Figure 1b (grey shaded area, normalised), spans 1.71 to 2.47 eV (500–720 nm) and simultaneously covers the Tr- and Lg-LSP modes (as highlighted by the grey area in Figure 1b, denoting the overlap region between S_p and the NRs' resonant absorbance).

The main results of our 2DES experiments are summarised in **Figure 2**, which presents four 2DES maps of the differential transmission signal ΔI as a function of excitation and detection energies (along the vertical and horizontal axes, respectively) at representative waiting times ($t_2 = 50$ fs, 100 fs, 500 fs, and 1 ps, from left to right). For each map, the integral over the excitation energies, equivalent to a broadband TA (differential transmission) spectrum,[56,57] is also shown (bottom panels, see also Figure S3, Supporting Information). The spectral structure of the maps displays two positive diagonal peaks and two positive cross peaks, with a negative modulation centered in the middle of the detection-energy spectrum. These features can be explained by considering that the typical nonlinear response of photoexcited plasmonic nanostructures arises from spectral modulations due to the shift and broadening of their optical resonances. Thus, in analogy with ultrafast TA spectra of Au NRs,[32,58,59] we attribute the signals in the low-detection-energy region (E_{det} below ≈2.1 eV) to the modulations of the Lg-LSP, while the photoinduced shift and broadening of the Tr-LSP predominantly affect the high-detection-energy region ($E_{\text{det}} > \approx 2.2$ eV). The 2DES signal exhibits, although to a lesser degree, also a dependence on the excitation energy (that is, cuts taken at different excitation energies are different). These variations with E_{exc} are primarily dominated by pump-pulse-selective mechanisms (i.e., different NR subsets respond distinctly, depending on the detuning of their resonances with respect to the pump photon energy,[32–34]) which take place also under broadband excitation. These effects explain the negative modulation observed around $E_{\text{exc}} \approx 2$ eV and $E_{\text{det}} < 1.8$ eV, which can be ascribed to the selective excitation of the NRs of lowest aspect ratio, whose Lg-LSP falls within this region (as indicated by the TEM analysis, see Figure 1c). Their contribution tends to skew the transient signal, bringing into the detection bandwidth an additional negative lobe of the Lg-LSP modulation at lower detection energies.[32]

In terms of spectral shape, from the early onset of the signal and throughout its entire dynamics, both the diagonal and the cross peaks exhibit significantly different lineshapes. At lower detection energies, the diagonal peak (bottom left in the maps) is markedly elongated along the diagonal, while the cross peak (top left, corresponding to excitation of the Tr-LSP) is more symmetric. In contrast, at higher detection energies, the diagonal peak (top right) appears nearly circular, while the cross peak (bottom right, corresponding to excitation of the Lg-LSP) is elliptical along the excitation axis (vertical). These lineshapes can be understood as reflecting the projections of the static absorbance (shown also in Figure 2, rightmost panel, for direct comparison) and the distinct broadening mechanisms of the Tr- and Lg-LSP steady-state lineshapes. In particular, pump photons at lower energies (E_{exc} up to ≈2 eV) resonantly interact with the NRs' Lg-LSP mode, which is highly sensitive to the rod length, hence exhibits strong inhomogeneous broadening. This produces elongated diagonal (bottom left) and cross peaks (bottom right), resulting from the convolution of narrower signals associated with inhomogeneously excited NR subsets. In contrast, excitation energies closer to the Tr-LSP ($E_{\text{exc}} > 2.2$ eV) produce a circular diagonal peak (top right), reflecting the homogeneous broadening of this mode, almost insensitive to the NR size. Although the excitation of the Tr-LSP is homogeneous, a slight elliptical lineshape is observed at the cross peak probing the Lg-LSP mode (top left), which reflects the projection of the Lg mode steady-state inhomogeneous broadening. This comprehensive picture of inhomogeneous versus homogeneous excitation and detection corroborates previous studies[46,47] and offers additional understanding beyond that achievable with narrower pulse bandwidths, restricted to the Lg-LSP.

To quantitatively characterise the lineshape differences in the 2DES maps, we examined the two diagonal peaks (highlighted

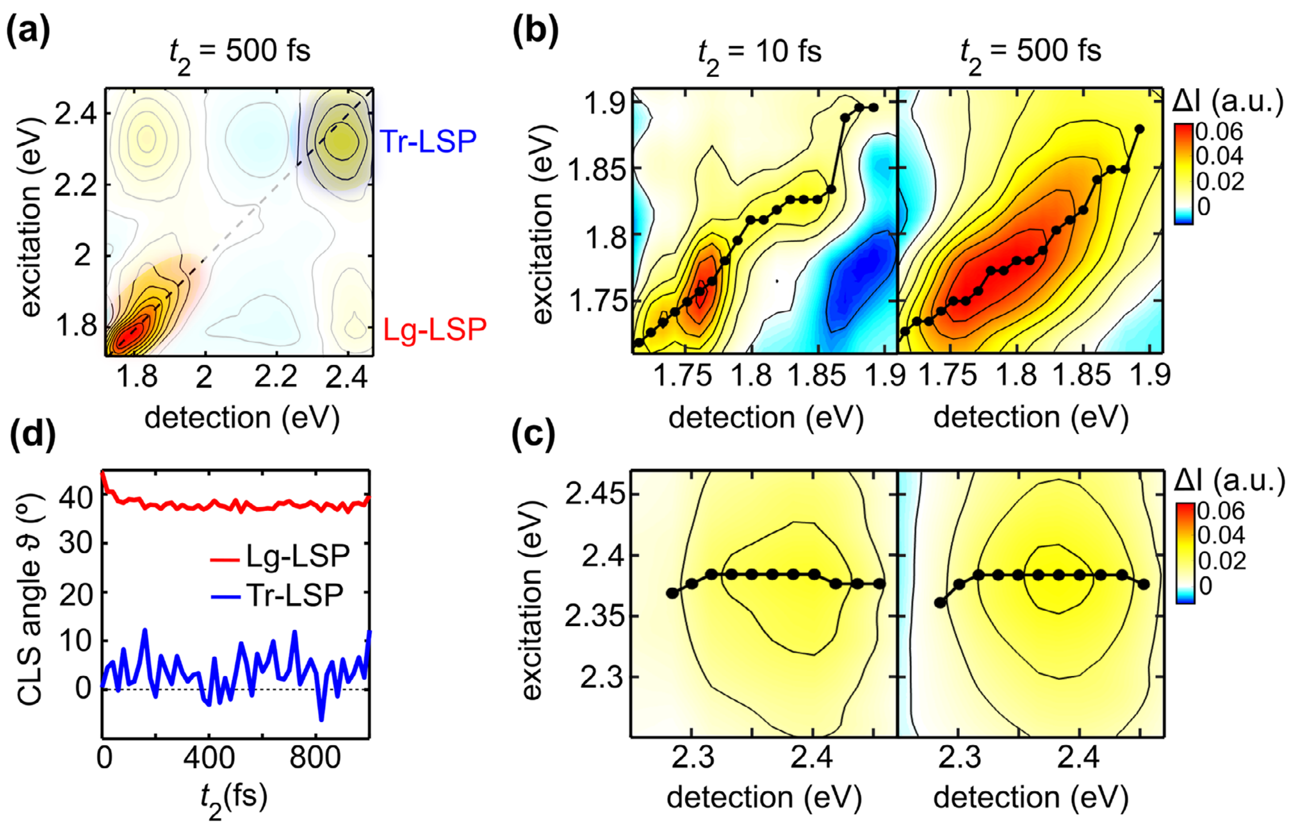

Figure 3. Central Line Slope analysis. a) Pure absorptive 2DES map at t_2 = 500 fs, where the diagonal peaks arising from the modulation of the Lg- (red) and Tr-LSP (blue) are highlighted. b) Pure absorptive 2DES maps at t_2 = 10 fs and 500 fs, cut around the Lg-LSP modulation region (from 1.71 to 1.91 eV). c) Same as (b) for the Tr-LSP peak (cut from 2.25 to 2.47 eV). In both panels (b) and (c), the black dots are obtained by using CLS algorithm. d) Temporal evolution of the CLS angle for the two peaks.

in blue and red in **Figure** 3a) and monitored their spectral shape using the Central Line Slope (CLS) analysis.[60–62] In this method, a 'central line' is extracted by tracking the peak maxima along the detection axis for each excitation energy, and a linear fit of this line yields its slope, denoted by the parameter ϑ. This slope quantifies the degree of spectral correlation between excitation and detection energies. A value of ϑ = 0°, with CLS points aligned horizontally, indicates an isotropic, circular lineshape, whereas ϑ = 45° corresponds to a perfectly diagonal feature. The main results of our CLS analysis are summarized in Figure 3.

In particular, Figure 3b,c display 2DES maps (recorded at t_2 = 10 fs and 500 fs) cut around the diagonal peaks, associated with modulations of the Lg- and Tr-LSP, respectively. The extracted CLS points are shown as black dots. The corresponding temporal dynamics of the CLS parameter ϑ for the two modulation peaks are presented in Figure 3d. As illustrated in Figure 3c, the high-energy peak maintains a nearly circular shape from the earliest times throughout the entire dynamics, with ϑ fluctuating ≈0°. These comparatively large fluctuations originate from the lower signal-to-noise ratio of the Tr-LSP modulation in the 2DES signal, which makes its CLS slope more susceptible to noise. By contrast, the Lg-LSP modulation peak appears markedly more elliptical along the diagonal (see black dots and line in Figure 3b). After an initial ultrafast evolution for $t_2 < 200$ fs (matching the timescales observed in a previous analysis[46]), the extracted CLS slope ϑ stabilizes at ≈37°. Noise-driven fluctuations are also present in this case, yet with a smaller amplitude, owing to the stronger 2DES signal associated with the Lg-LSP. The relatively constant CLS angles extracted for both peaks (0° and 37°, respectively) indicate that the 2DES lineshapes mostly reflect the static broadening of the sample absorbance peaks (homogeneous for the Tr-LSP, inhomogeneous for the Lg-LSP), a steady-state mechanism inherent to the polydisperse NR ensemble. The data show no indications of spectral diffusion, as typically observed in molecular systems. The only feature not attributable to static broadening is the (relatively minor) ultrafast decay of ϑ for the Lg-LSP within the first few hundred femtoseconds, which we interpreted as linked instead to the dynamic evolution of the integrated 2DES spectra in the 1.71–2 eV region (Figure 2, see also Figure S3, Supporting Information). Indeed, in this spectral range, the positive lobe broadens toward higher energies, as highlighted by the grey circles in the bottom panels of Figure 2, which trace the isosbestic (zero-crossing) point, blueshifting over time from ≈1.92 eV (645 nm) up to 2 eV (620 nm) at 1 ps.

To gain deeper insight into the origin of the ultrafast dynamic behavior observed in the 2DES maps and elucidate the photoinduced electronic mechanisms governing the spectro-temporal evolution of the nonlinear optical signal, we developed a quantitative model of the system's nonequilibrium optical response.

To reduce numerical complexity, our calculations modelled a broadband TA experiment rather than a full 2DES measurement, which fell beyond the scope of this work (refer to Section S4, Supporting Information for further details). However, given the correspondence between the differential transmittance in a broadband TA experiment and the 2DES signal integrated over the excitation energy[56,57] (see also Figure S3, Supporting Information), the conclusions and insights derived from our model rigorously apply to 2DES measurements as well. In particular, we adopted previously reported approaches[20,63] to describe the transient nonlinearities of metallic nanostructures, and further refined them to incorporate the effects of the ultrabroadband excitation and the NRs' resonant absorption, which are distinctive features of the system under study.

The photoexcited hot carriers governing the nonlinear optical response of plasmonic nanostructures in the ultrafast regime can be associated with a generic nonequilibrium energy occupancy distribution $f(E,t) = f_0(E) + \Delta f(E,t)$, where $f_0(E) = [1+e^{(E-E_F)/k_B\Theta_0}]^{-1}$ is the equilibrium Fermi–Dirac (FD) distribution, E_F the Au Fermi level, k_B the Boltzmann constant, Θ_0 the room temperature. Modifications in the metal electron distribution lead to changes in the allowed optical transitions, which translate into broadband modulations of the material permittivity ($\Delta\varepsilon$), affecting the system's transient optical response. To first describe the ultrafast dynamics of photoexcited hot carriers, we employed the so-called Extended Two-Temperature Model (E2TM).[64] This is a thermodynamic rate-equation model describing the evolution of nonequilibrium electronic and phononic states in plasmonic nanostructures in terms of three energetic degrees of freedom: (i) Δf_{NT}, the deviation from the equilibrium distribution f_0 due to a fraction of photoexcited carriers referred to as 'nonthermal' (NT), as their energy spectrum markedly differs from a FD-like one and extends to energies above E_{F} up to the pump-pulse photon energies; (ii) Θ_{E}, the temperature of a 'thermalized' (T) portion of hot carriers that populate nonequilibrium states near E_{F}, whose energy distribution differs by Δf_{T} from f_0, but can be described by a FD-like function at a higher temperature Θ_{E}, i.e. $f(E, \Theta_{\mathrm{E}}) = [1+e^{(E-E_F)/k_B\Theta_E}]^{-1}$; and (iii) Θ_{L}, the lattice temperature of the nanostructure. By interlinking Δf_{NT}, $\Theta_{\mathrm{E},}$ and Θ_{L} in a set of differential equations with coupling coefficients that account for the electron–electron and electron-phonon scattering mechanisms (see Experimental Section under heading "Numerical Modelling"), the E2TM tracks the flow of the excess energy delivered by the incident photons through the metal electrons and lattice over time. Specifically, integrating the E2TM yields the variations in the electron energy occupancy probability, which, for the NT and T hot carriers, respectively, are expressed as follows:[63]

$$\Delta f_{\mathrm{NT}}(E, t) = \frac{1}{A}\Delta_{\mathrm{NT}}(E)\int_{-\infty}^{t} P_{\mathrm{abs}}(t')\, e^{(t-t')/\tau(E)}\mathrm{d}t' \qquad (1)$$

$$\Delta f_{\mathrm{T}}(E, t) = f\left[E, \Theta_E(t)\right] - f\left[E, \Theta_0\right] \qquad (2)$$

with A, $P_{\mathrm{abs},}$ and τ defined in the Experimental Section under heading "Numerical Modelling". While the thermal contribution Δf_{T} is localized mostly around the Fermi level, Δf_{NT} is characterized, via $\Delta_{\mathrm{NT}}(E)$, by a spectral shape involving energies as high as the absorbed photon energy. We formulated this term as:

$$\Delta_{\mathrm{NT}}(E) = \int S_{\mathrm{p}}(h\nu)\, \mathrm{Abs}^i(h\nu)\, \delta_{\mathrm{NT}}(E,h\nu)\, \mathrm{d}h\nu \qquad (3)$$

where $\delta_{\mathrm{NT}}(E, h\nu)$ is a double-step-like function[63] whose energy extension from E_F equals the impinging photon energy $h\nu$, $S_{\mathrm{p}}(h\nu)$ is the power spectral density of our pump pulses, and $\mathrm{Abs}^i(h\nu)$ the absorbance of the i-th NR subset within the sample (see also experimental section heading "Numerical Modelling"). Notably, the expression we here propose for $\Delta_{\mathrm{NT}}(E)$ accurately takes into account the relevant electronic states that, upon ultrabroadband photoexcitation, contribute to the optical modulation (see also Figure S4, Supporting Information). We then applied consolidated approaches[65] to evaluate the effects of a nonequilibrium carrier distribution on the Au permittivity, and hence on the transient optical behavior of an individual subset. Finally, the calculations were repeated for all the considered NR subsets, and, analogously to the static response (Figure 1c), the overall nonequilibrium response was determined as a weighted sum of each subset's contribution, based on the relative occurrence estimated from TEM analysis.

The outcome of our model is shown in **Figure** 4b, which presents the simulated differential transmission spectra ΔT/T induced by a broadband pump pulse as a function of probe photon energy and pump-probe delay, and compares them with the corresponding broadband TA measurement (Figure 4a) using the same pump/probe pulses as for 2DES. In agreement with the spectra of the integrated 2DES signal (Figure 2, bottom), the measured ΔT/T exhibits two main positive lobes (centered at ≈1.8 eV and ≈2.4 eV), separated by a negative modulation region (between 2 and ≈2.3 eV). The signal reaches its maximum amplitude within ≈200 fs, followed by a decay over a few ps. Simulations accurately reproduce the spectro-temporal dynamics of the experimental ΔT/T, including a distinctive ultrafast sign change at the earliest onset of the dynamics in the 1.9–2 eV region (highlighted by the dashed box in Figure 4, see also Figures S5 and S6, Supporting Information for a detailed view and a temporal cut).

This peculiar feature, previously analyzed for comparable metallic systems,[63,66] can be rationalised by disentangling the simulated ΔT/T spectra into the distinct contributions arising from NT and T electrons (Figure 4c,d, respectively). In agreement with previous reports, NT carriers contribute to the optical modulation within the first few hundred femtoseconds, when their relaxation is completed following electron–electron scattering. Conversely, the ΔT/T due to thermal carriers exhibits a delayed onset, is larger in amplitude (note the magnification factor for the NT signal in Figure 4c), and lasts a few picoseconds, following electron-phonon scattering. In the specific spectral region under analysis (see also Figure S5, Supporting Information), the two contributions to ΔT/T have opposite signs, and their spectro-temporal interplay explains the ultrafast sign inversion observed at these probe energies.

Note that, in this picture, the time of sign inversion correlates directly with the electron–electron scattering time, τ_{ee}. Moreover, the transfer of photo-absorbed excess energy from NT to T hot carriers is also reflected in the spectral domain, in a two-fold manner. First, at early times, the ΔT/T signal at lower detection energies predominantly arises from higher-energy carriers

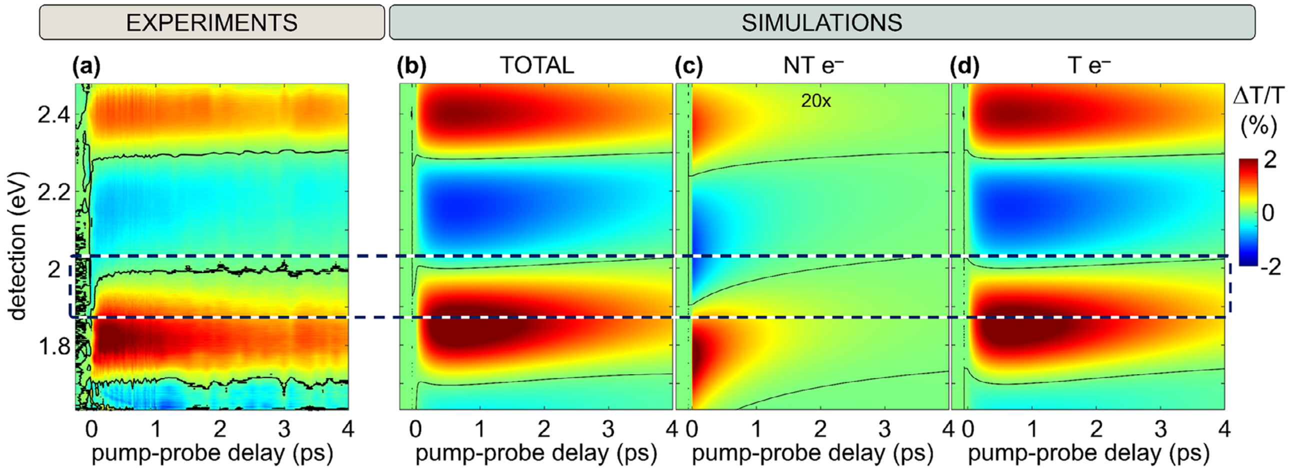

Figure 4. Broadband TA spectroscopy. Experimental a) and simulated b) maps of the differential transmittance ΔT/T of the plasmonic NRs in solution upon ultrabroadband photoexcitation. The simulated map is further disentangled in the contributions arising from nonthermal (NT e⁻, panel c) and thermalized hot electrons (T e⁻, panel d). The nonthermal contribution c) is magnified by a factor of 20 for better reading. Isosbestic curves (signal equal to zero) are also shown as black lines. The dashed box marks the spectral window where the ultrafast (< 200 fs) sign inversion takes place. Simulations were performed for a pump fluence of ≈200 μJ/cm^2, i.e., twice the estimated experimental value.

(hot holes), as demonstrated in previous studies,[67] while carriers closer to the Fermi level induce stronger modulations at higher detection energies. Second, as predicted by Fermi liquid theory, τ_{ee} scales inversely with the square of the pump photon energy, meaning that carriers photogenerated by higher excitation energies relax more rapidly.

To correlate the sign inversion of the broadband measured and simulated TA maps and the discussion on τ_{ee} with the results of the CLS analysis and the trends observed in Figure 2, we further investigated the temporal evolution of the signals extracted directly from the 2DES maps. **Figure 5a** shows selected temporal traces as a function of t_2, obtained by integrating the 2DES maps over the excitation axis at four fixed detection energies, corresponding to the peaks in the TA maps (1.82, 2.15, and 2.4 eV) and to a representative value within the sign inversion region (1.9–2 eV). In particular, the dynamics at 1.925 eV (purple line) reveals precisely the evolution predicted by the model, with an ultrafast (<200 fs) inversion from negative to positive, followed by a positive plateau and a decay back to equilibrium within a few picoseconds.

To selectively probe the dynamic effects influenced by electron–electron relaxation, we then extracted from the 2DES maps the temporal traces at a fixed excitation energy (set at 2.41 eV, i.e., at the Tr-LSP static peak, ensuring homogeneous excitation within the sample), while varying the detection energy in the 1.9–2 eV range. All traces in Figure 5b exhibit the expected dynamics, featuring an ultrafast sign change within ≈200 fs. Notably, the rate of the sign inversion, which reflects the relaxation of NT carriers, varies with the detection energy. As shown more clearly by the normalised curves (Figure S7, Supporting Information), higher detection energies correspond to lower rates (with the zero-crossing occurring at longer delays) across the entire considered bandwidth. By fitting the 2DES traces (Figure S8, Supporting Information), we estimated time constants increasing from ≈85 fs (rate 0.012 fs^{-1}) at the lowest detection energy E_{det} = 1.91 eV, to ≈170 fs (rate 0.006 fs^{-1}) at the highest, 1.982 eV. The trend of the extracted time constants as a function of the detection energy is summarised in Figure S9 (Supporting Information).

Finally, to inspect the NT carrier relaxation as a function of the excitation energy, we extracted temporal traces from the 2DES maps at fixed detection energy, set to 1.925 eV (Figure 5c). Excitation energies were selected in a portion of the pump pulse bandwidth to ensure comparable excitation levels. Notably, the intrinsic broadband nature of 2DES experiments provides direct access to the influence of the excitation energy on τ_{ee}. The extracted traces exhibit a clear dependence on the excitation energy, following the predicted trend qualitatively, as further emphasized in Figure S7 (Supporting Information) after normalisation. Lower excitation energies, generating NT carriers with a narrower energy content around the Fermi level (see sketch in Figure S4, Supporting Information), correspond to slower dynamics (i.e., a reduced scattering rate), delaying the energy transfer to thermal hot carriers. The time constants obtained by fitting these 2DES temporal cuts decrease from ≈100 fs (corresponding rate 0.01 fs^{-1}) down to ≈30 fs (rate of 0.033 fs^{-1}) over the excitation energies considered (refer to Figure S9, Supporting Information for the full trend).

All these observations support our interpretation that the energy relaxation from NT to T carriers governs the spectrotemporal evolution of the 2DES signals in the detection region where the CLS analysis of the Lg-LSP modulation peak was performed (Figure 3b). This region also corresponds to the detection energies involved in the transient shift of the isosbestic point highlighted in Figure 2. In light of these arguments, we attribute the initial ultrafast dynamics of the CLS parameter to this carrier internal relaxation, which also drives the variation of the spectral contributions to the modulation, resulting in the apparent spectral deformation of the Lg-LSP modulation peak. Since the NT/T hot carriers interplay occurs in the specific spectral bandwidth (illustrated in Figure 4c,d), the Tr-LSP remains unaffected by this transient

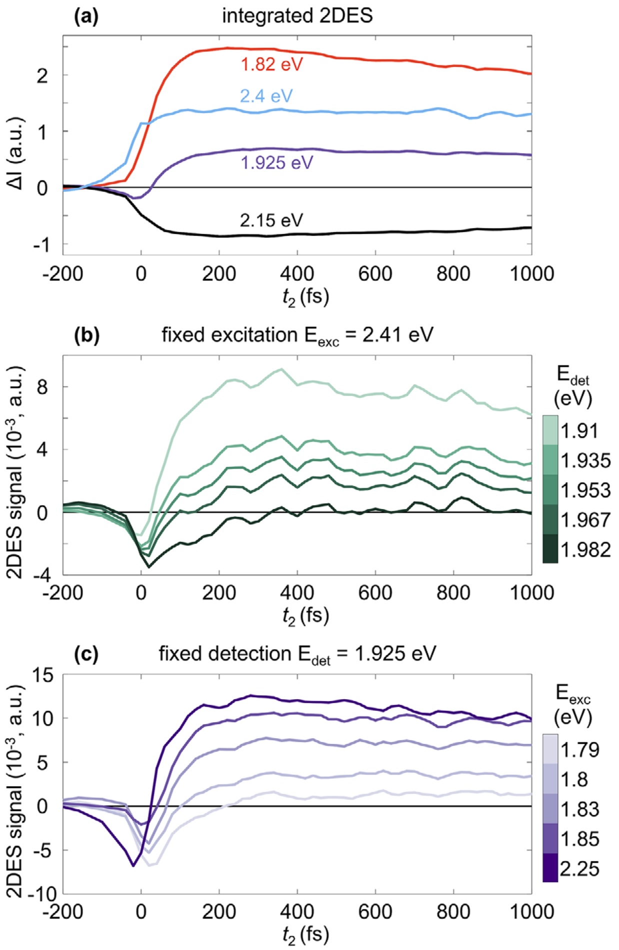

Figure 5. Spectro-temporal dynamics from 2DES maps. a) Temporal dynamics of the 2DES signal integrated over the excitation axis for selected detection energies (1.82, 1.925, 2.15, 2.4 eV). b) 2DES signal ΔI at a fixed excitation energy (2.41 eV, i.e., corresponding to the Tr-LSP absorption peak) for varying detection energies between 1.91 and 1.98 eV. c) 2DES signal ΔI at a fixed detection energy (1.925 eV, i.e., within the isosbestic points region) at varying excitation energies.

mechanism, consistent with the outcomes of our CLS analysis (Figure 3d).

3. Conclusion

In summary, this study examined the ultrafast broadband optical response of colloidal plasmonic nanorods using 2DES, a powerful time- and energy-resolved technique that has seen only limited application to metallic nanostructures so far. The ultrabroadband laser pulses (1.71–2.47 eV) enabled the simultaneous interrogation of both the transverse and the longitudinal plasmon resonances of the Au nanorods, while their ultrashort duration (<15 fs) allowed us to study the photoinduced dynamic processes, including electron–electron scattering, with high temporal resolution. In the spectral domain, the 2DES maps reflected both the inhomogeneous and homogeneous broadening of the static LSP modes (longitudinal and transverse, respectively). A central line slope analysis was applied to quantify the broadening inherent to the polydisperse sample, complementing the correlated TEM analysis. Together with the corresponding off-diagonal projections, the observed modulation signals encompassed all combinations of homogeneous and pump-preferential interactions, underscoring the role of spectral selectivity at the excitation stage. In the temporal domain, a quantitative model of hot-carrier-mediated optical nonlinearities guided our investigation and accurately elucidated the observed transient features in terms of the dynamic interplay between nonthermal and thermal fractions of the photoinduced carriers. Notably, our model consistently incorporated the sample polydispersity, the broadband character of the excitation, and the resonant absorption of the nanostructures, thereby providing a robust framework for describing the photogeneration and ultrafast dynamics of plasmonic hot carriers. We further connected the model predictions, broadband TA measurements, and 2DES experiments to identify the fingerprint of electron–electron scattering events in the ultrafast evolution of the measured signals, attributing the spectral changes around the Lg-LSP peak to this mechanism. As a whole, our analysis provides a comprehensive interpretation of the ultrafast features of 2DES maps collected from a prototypical plasmonic nanostructure. The unique combination of temporal and spectral resolution of this advanced spectroscopic technique, which we leveraged to extract information on electron–electron scattering, holds promise for tracking a range of ultrafast processes involving plasmonic hot carriers, such as energy transfer to molecular adsorbates or semiconductors. Our strategy can also be extended to more elaborate plasmonic nanostructures, e.g., multi-modal complex morphologies, where tailored models, complementary TA measurements, careful consideration of inhomogeneous broadening, and appropriate tuning of the pulse spectrum[46] would support the interpretation of the resulting 2DES maps. We envisage that this study will support the broader application of 2DES in characterizing ultrafast light-matter interactions in more complex plasmon-based systems, including antenna-reactors and strongly-coupled hybrids.

4. Experimental Section

Sample Preparation: Au NRs were synthesized by a seed-growth method, adapted from a previously developed protocol.[68] All the glassware was carefully washed with aqua regia (3:1 mixture of hydrochloric acid (HCl) and nitric acid (HNO_3)) and rinsed with Milli-Q water before use. Briefly, two different solutions were prepared: a seed solution and a growth solution. In the seed solution, 1 mL of 0.1 mᴍ CTAB in Milli-Q water was mixed with 43 µL of 10 mᴍ $HAuCl_4$ until reaching a yellow/orange color. Afterward, 60 µL of a freshly prepared ice-cooled $NaBH_4$ solution (1.89 mg in 0.5 mL in Milli-Q water) was added to the mixture, and maintained under vigorous stirring for 30 min at 30 °C. For the growth solution, 0.72 g of CTAB and 0.098 g of sodium oleate were dissolved in 20 mL Milli-Q water under vigorous stirring at 90°C for 90 min. After cooling down at 30 °C, the mixture was diluted with 20 mL Milli-Q water, and 2 mL of a 10 mᴍ $HAuCl_4$ solution was added, keeping the solution under stirring at 30 °C for 90 min, time after which it turned from yellow/orange to transparent. Then, 168 µL of 37% v/v HCl was added to the growth solution, and after 15 min under stirring, 64 µL of 0.1 mᴍ ascorbic acid solution and 32 µL of the prepared seed solutions were added. The reactive mixture was maintained under vigorous stirring for 30 s, then it was left for 12 h at 30 °C. The obtained Au NRs were purified by removing the supernatant containing CTAB excess after repeated 15 min centrifugation cycles at 6000 rpm. The pellet was resuspended in fresh Milli-Q water and stored at 4 °C.

The Au NRs concentration obtained was 0.07 mg mL^{-1}, evaluated through inductively coupled plasma optical emission spectroscopy.

Two-Dimensional Electronic Spectroscopy Experiments: 2DES exploits a sequence of three delayed broadband pulses that interact with a system, resulting in the emission of a third-order nonlinear signal as a function of the delays between the pulses. The first and the second pulse act as the pump excitation, and the delay between them is referred to as 'coherence time' and labeled t_1. The third pulse acts as the probe, and the delay between the second and third pulse is called 'waiting time', labeled t_2. The nonlinear signal emitted by the system after the interaction with the probe pulse propagates along the delay time t_3, called 'detection time'.[69] Such a signal is spectrally resolved by a spectrometer, which performs a Fourier transform with respect to t_3, providing the detection frequency axis ω_3. The signal is then processed by performing a Fourier transform with respect to the delay t_1, from which the excitation frequency axis ω_1 is generated. The 2DES data can be visualized as a sequence of maps that correlate excitation and detection photon energies for each value of the waiting time t_2.

In this work, a degenerate configuration of the pulses was employed, which are generated by a non-collinear optical parameter amplifier (NOPA) pumped by an amplified Ti: Sapphire laser that emits 100-fs pulses centered at 800 nm with 1-kHz repetition rate.[70] The output of the NOPA produces pulses with a spectrum ranging from 1.71 to 2.47 eV. Such pulses are then temporally compressed with a pair of chirped mirrors down to 15 fs. 2DES experiments are performed in the partially collinear geometry, where the two pump pulses propagate collinearly, and the nonlinear signal emitted by the system propagates along the probe direction (self-heterodyned detection). This experimental geometry allows for direct detection of the so-called 'purely absorptive' signal, where the interpretation of the positive and negative peaks is the same as $\Delta T/T$ in a TA experiment.[71–73] To generate the three pulses from the NOPA, a beam splitter was used to separate the pump and the probe optical paths. A mechanical translation stage was placed along the probe path to control the delay t_2. Delay t_1 is generated and controlled by inserting in the pump optical path a birefringent common-path interferometer known as the Translating-Wedges-Based Identical pulses encoding System (TWINS).[74] A schematic of the experimental apparatus is shown in Figure S2 (Supporting Information). The experiment was performed using ≈100 µJ cm^{-2} pump fluence, with relative perpendicular polarization between pump and probe pulses to suppress pump scattering, at room temperature. The sample was measured in a 200-µm fused silica cuvette at a NR concentration of 0.35 mg mL^{-1}, higher than that used for the static absorbance measurements (0.07 mg mL^{-1}), in order to enhance signal-to-noise ratio, while still avoiding inter-particle coupling or any measurable aggregation effects in the solution. Delay t_1 was scanned from −30 to 250 fs, and delay t_2 was scanned from −250 to 5 ps. The same experimental apparatus can be easily converted into a broadband TA setup by fixing the delay $t_1 = 0$ fs. In this case, the 'population time' that characterizes the time axis in a TA experiment is substituted by the delay t_2. The broadband TA experiment is performed maintaining the same experimental settings, in terms of beam polarizations, delay steps, and excitation fluence, which were adopted for the 2DES experiment.

Numerical Modelling: To reproduce the static response of the sample, information on the NRs' size dispersion was combined with an analytical description of single nanoparticles optical behavior. The former was obtained by analyzing a TEM image of the experimental sample, extracting the widths, lengths, and ARs of a statistically significant number of nano-objects (≈680 in total). The NRs were then grouped by size into 100 subsets, which were assumed to be monodisperse, each identified by a specific width (5 sub-groups, corresponding to a size resolution of ≈2.5 nm) and AR (20 sub-groups, with ≈0.15 resolution, determining the length of the NR), with a given relative occurrence within the sample. For the optical response of a single i-th subset, an analytical method incorporating retardation effects[55] was employed to compute the extinction cross-section σ^i_{ext} of an individual NR embedded in water (refractive index 1.4). The Au static permittivity $\varepsilon^0(\lambda)$ was described using an analytical expression[75] fitted to experimental data,[76] with the Drude damping factor increased (3-fold) compared to its bulk value[75] to account for residual size dispersion (the TEM image analysis involves only a portion of the entire sample) and additional absorption/scattering possibly due to, e.g., material imperfections. To mimic the randomized orientation of the colloidal NRs in solution, an effective polarization angle was introduced, with the best agreement with experiments achieved at 65° for all the subsets. Each NR subset was treated as an ensemble of identical nanoparticles, with its transmittance calculated as $T^i = e^{-\sigma^i_{\text{ext}} N^i L}$, where L is the cuvette length and N^i the concentration of the i-th subset, expressed as the product of its occurrence and the total sample concentration (set to 80% of its nominal value to best reproduce the measurement). The overall sample absorbance was then obtained by summing the contributions of all subsets, each defined as $\text{Abs}^i = -\log_{10}(T^i)$.

In the ultrafast regime, a model was developed to reproduce the broadband TA experiments (simulations of the excitation-resolved 2DES signals fall beyond the scope of this study). In particular, to simulate the sample transient optical response, previous approaches[20,63] were built upon and further refined them to account for the system's distinctive ultrabroadband excitation and resonant absorption, alongside the aforementioned size dispersion. The first ingredient of our model is the ultrafast dynamics of plasmonic hot carriers. To describe this dynamics, the so-called Extended Two-Temperature Model (E2TM)[64] was employed, which characterizes the evolution of nonequilibrium electronic and phononic states in plasmonic nanostructures by three variables: (i) Δf_{NT}, the variation of the electron occupancy distribution due to a 'nonthermal' fraction of the carrier population; (ii) Θ_{E}, an increased electronic temperature of 'thermal' carriers, associated with an excited Fermi–Dirac distribution; and (iii) Θ_{L}, the metal lattice temperature. The temporal evolution of these three variables is governed by a set of differential equations expressed as follows:

$$\frac{\partial \Delta f_{\text{NT}}(E,t)}{\partial t} = -\frac{\Delta f_{\text{NT}}}{\tau_{\text{ee}}} - \frac{\Delta f_{\text{NT}}}{\tau_{\text{ep}}} + \frac{1}{A}\Delta_{\text{NT}}(E)\, P_{\text{abs}}(t) \tag{4}$$

$$C_{\text{E}}\frac{\text{d}\Theta_{\text{E}}}{\text{d}t} = -G\,(\Theta_{\text{E}} - \Theta_{\text{L}}) + \int P_{\text{abs}}(t')\, H_{\text{ee}}(t - t')\,\text{d}t' \tag{5}$$

$$C_{\text{L}}\frac{\text{d}\Theta_{\text{L}}}{\text{d}t} = +G\,(\Theta_{\text{E}} - \Theta_{\text{L}}) + \int P_{\text{abs}}(t')\, H_{\text{ep}}(t - t')\,\text{d}t' \tag{6}$$

The coefficients above regulate the energy exchange following photo-absorption: τ_{ee} and τ_{ep} (often used to define a total relaxation time $\tau = \tau_{\text{ee}}\tau_{\text{ep}}/(\tau_{\text{ee}} + \tau_{\text{ep}})$) govern the relaxation of nonthermal electrons via electron–electron and electron-phonon scattering, respectively; G is the electron-phonon coupling; C_{E} and C_{L} denote the thermal electron and lattice heat capacities. The term P_{abs} represents the pump electromagnetic power density absorbed by the metal nanostructure, estimated from static simulations, while H_{ee} and H_{ep} are driving kernels derived from more rigorous approaches.[77] Finally, $\Delta_{\text{NT}}(E)$ is the initial energy spectrum of nonthermal carriers, and $A = \int_E \text{EDOS}(\text{E})\Delta_{\text{NT}}(\text{E})\text{dE}$ is a normalization constant ensuring energy conservation,[63] with DOS(E) the Au electronic density of states, taken from ab-initio calculations.[78] Notably, in our model, $\Delta_{\text{NT}}(E)$ accounts for both the broadband character of the pump excitation and the spectral dispersion of the sample absorption (see Equation (3)). Further details on the E2TM can be found elsewhere.[20,64] To translate the dynamics of the hot carriers and the lattice temperature into transient modulations of the sample optical response, a semi-classical model for the Au thermo-modulational nonlinearities[65] was employed and computed the photoinduced variations of the metal permittivity, $\Delta\varepsilon(\lambda,t)$. In essence, both nonthermal and thermal carriers contribute to modify the electron energy occupancy distribution via energy- and time-dependent terms (refer also to Equations (1) and (2)). In turn, owing to Pauli blocking, a nonequilibrium electronic distribution affects the metal interband transitions (at the L- and X-point in the first Brillouin zone, in our model), a process described as a modification of the imaginary part of the permittivity (its real counterpart being given by Kramers–Kronig relations). In contrast, an increased lattice temperature alters the Drude term of the permittivity by varying the damping factor[79] and plasma frequency.[80] A more extensive discussion of these mechanisms can be found elsewhere.[20] The modified metal permittivity $\varepsilon(\lambda, t) = \varepsilon^0 + \Delta\varepsilon$, evolving in time according to the dynamics of the E2TM degrees of freedom, serves as input for computing the system transient transmittance, iterating over time the same calculations used in the static regime (considering the cuvette length of 200 μm and concentration used in the ultrafast experiments). To incorporate the sample size dispersion also in the ultrafast response, these calculations were repeated for all the NR subsets at each time step, accounting for their relative occurrence. The total transient transmittance was then determined by summing each subset's nonequilibrium transmittance. Further details on the numerical implementation of our model can be found in the Section S4 (Supporting Information).

Supporting Information

Supporting Information is available from the Wiley Online Library or from the author.

Acknowledgements

A.S. and M.R. contributed equally to this work. M.M. acknowledges financial support from the ERC-StG ULYSSES grant agreement no. 101077181 funded by the European Union. A.S, G.C., G.D.V., and M.M. acknowledge financial support from the European Union's NextGenerationEU Programme with the I-PHOQS Infrastructure [IR0000016, ID D2B8D520, CUP B53C22001750006] "Integrated infrastructure initiative in Photonic and Quantum Sciences" and from the METAFAST project that received funding from the European Union Horizon 2020 Research and Innovation programme under grant agreement no. 899673. G.D.V. and M.M. acknowledge financial support from European Union – Next Generation EU – PNRR – M4C2, investimento 1.1– "Fondo PRIN 2022" under the projects HOTMETA (HOT-carrier METasurfaces for Advanced photonics, ID 2022LENW33, CUP:D53D2300229 0006) and PhotoControl (Molecular Control of PhotoProtection in Photosynthetic Organisms, ID 2022N8PBLM, CUP: D53D2300919 0001). A.S. and G.D.V. acknowledge the European Union's Horizon Europe research and innovation programme under the Marie Skłodowska–Curie Action PATHWAYS HORIZON-MSCA-2023-PF-GF grant agreement no. 101153856. Views and opinions expressed are, however, those of the author(s) only and do not necessarily reflect those of the European Union or the European Research Council. Neither the European Union nor the granting authority can be held responsible for them.

Open access publishing facilitated by Politecnico di Milano, as part of the Wiley - CRUI-CARE agreement.

Conflict of Interest

The authors declare no conflict of interest.

Data Availability Statement

The data that support the findings of this study are available from the corresponding author upon reasonable request.

Keywords

electron dynamics, hot electrons, two-dimensional electronic spectroscopy, ultrafast plasmonics

Received: October 6, 2025
Revised: December 15, 2025
Published online:

[1] J. A. Schuller, E. S. Barnard, W. Cai, Y. C. Jun, J. S. White, M. L. Brongersma, *Nat. Mater.* **2010**, *9*, 193.
[2] L. M. Liz-Marzán, C. J. Murphy, J. Wang, *Chem. Soc. Rev.* **2014**, *43*, 3820.
[3] P. K. Jain, X. Huang, I. H. El-Sayed, M. A. El-Sayed, *Acc. Chem. Res.* **2008**, *41*, 1578.
[4] S. Lal, S. Link, N. J. Halas, *Nat. Photonics* **2007**, *1*, 641.
[5] H. A. Atwater, A. Polman, *Nat. Mater.* **2010**, *9*, 205.
[6] S. A. Maier, *Plasmonics: Fundamentals and Applications*, 1st ed., Springer US, New York, NY, **2007**.
[7] A. Manjavacas, J. G. Liu, V. Kulkarni, P. Nordlander, *ACS Nano* **2014**, *8*, 7630.
[8] R. Sundararaman, P. Narang, A. S. Jermyn, W. A. Goddard Iii, H. A. Atwater, *Nat. Commun.* **2014**, *5*, 5788.
[9] J. B. Khurgin, *Faraday Discuss.* **2019**, *214*, 35.
[10] J. G. Liu, H. Zhang, S. Link, P. Nordlander, *ACS Photonics* **2018**, *5*, 2584.
[11] M. L. Brongersma, N. J. Halas, P. Nordlander, *Nat. Nanotechnol.* **2015**, *10*, 25.
[12] M. Kauranen, A. V. Zayats, *Nat. Photonics* **2012**, *6*, 737.
[13] R. B. Davidson II, A. Yanchenko, J. I. Ziegler, S. M. Avanesyan, B. J. Lawrie, R. F. Haglund Jr., *ACS Photonics* **2016**, *3*, 1477.
[14] P. Narang, R. Sundararaman, H. A. Atwater, *Nanophotonics* **2016**, *5*, 96.
[15] E. Cortés, W. Xie, J. Cambiasso, A. S. Jermyn, R. Sundararaman, P. Narang, S. Schlücker, S. A. Maier, *Nat. Commun.* **2017**, *8*, 14880.
[16] P. Christopher, H. Xin, S. Linic, *Nat. Chem.* **2011**, *3*, 467.
[17] Y. Zhang, S. He, W. Guo, Y. Hu, J. Huang, J. R. Mulcahy, W. D. Wei, *Chem. Rev.* **2018**, *118*, 2927.
[18] L. V. Besteiro, X.-T. Kong, Z. Wang, G. Hartland, A. O. Govorov, *ACS Photonics* **2017**, *4*, 2759.
[19] J. Khurgin, A. Y. Bykov, A. V. Zayats, *eLight* **2024**, *4*, 15.
[20] A. Schirato, M. Maiuri, G. Cerullo, G. Della Valle, Ultrafast hot electron dynamics in plasmonic nanostructures: experiments, modelling, design, **2023**, *12*, 1.
[21] J. Aizpurua, M. Ashfold, F. Baletto, J. Baumberg, P. Christopher, E. Cortés, B. de Nijs, Y. Diaz Fernandez, J. Gargiulo, S. Gawinkowski, N. Halas, R. Hamans, B. Jankiewicz, J. Khurgin, P. V. Kumar, J. Liu, S. Maier, R. J. Maurer, A. Mount, N. S. Mueller, R. Oulton, M. Parente, J. Y. Park, J. Polanyi, J. Quiroz, S. Rejman, S. Schlücker, Z. Schultz, Y. Sivan, G. Tagliabue, et al., *Faraday Discuss.* **2019**, *214*, 123.
[22] M. Conforti, G. Della Valle, *Phys. Rev. B* **2012**, *85*, 245423.
[23] R. W. Boyd, Z. Shi, I. De Leon, *Opt. Commun.* **2014**, *326*, 74.
[24] A. V. Krasavin, P. Ginzburg, A. V. Zayats, *Laser Photonics Rev.* **2018**, *12*, 1700082.
[25] M. Maiuri, M. Garavelli, G. Cerullo, *J. Am. Chem. Soc.* **2020**, *142*, 3.
[26] A. M. Brown, R. Sundararaman, P. Narang, A. M. Schwartzberg, W. A. Goddard, H. A. Atwater, *Phys. Rev. Lett.* **2017**, *118*, 087401.
[27] L. V. Besteiro, P. Yu, Z. Wang, A. W. Holleitner, G. V. Hartland, G. P. Wiederrecht, A. O. Govorov, *Nano Today* **2019**, *27*, 120.
[28] E. Y. Santiago, L. V. Besteiro, X.-T. Kong, M. A. Correa-Duarte, Z. Wang, A. O. Govorov, *ACS Photonics* **2020**, *7*, 2807.
[29] C. Voisin, N. Del Fatti, D. Christofilos, F. Vallée, *J. Phys. Chem. B* **2001**, *105*, 2264.
[30] G. V. Hartland, *Chem. Rev.* **2011**, *111*, 3858.
[31] A. Crut, P. Maioli, N. Del Fatti, F. Vallée, *Chem. Soc. Rev.* **2014**, *43*, 3921.
[32] X. Wang, Y. Guillet, P. R. Selvakannan, H. Remita, B. Palpant, *J. Phys. Chem. C* **2015**, *119*, 7416.
[33] W.-Y. Chiang, A. Bruncz, B. Ostovar, E. K. Searles, S. Brasel, G. Hartland, S. Link, *J. Phys. Chem. C 127*, **2023**, 21176.
[34] A. Schirato, L. Moretti, E. Lacroce, L. Polito, F. Rossi, G. Della Valle, M. Maiuri, *J. Phys. Chem. C* **2024**, *128*, 2551.

[35] S. Mukamel, *Principles of Nonlinear Optical Spectroscopy*, Oxford University Press, New York **1995**.
[36] E. Fresch, F. V. A. Camargo, Q. Shen, C. C. Bellora, T. Pullerits, G. S. Engel, G. Cerullo, E. Collini, *Nature Reviews Methods Primers* **2023**, *3*, 84.
[37] T. Nagahara, F. V. A. Camargo, F. Xu, L. Ganzer, M. Russo, P. Zhang, A. Perri, G. de la Cruz Valbuena, I. A. Heisler, C. D'Andrea, D. Polli, K. Müllen, X. Feng, Y. Mai, G. Cerullo, *Nano Lett.* **2024**, *24*, 797.
[38] S. Dhamija, M. Son, *Chemical Physics Reviews* **2024**, *5*, 041309.
[39] V. Petropoulos, P. S. Rukin, F. Quintela, M. Russo, L. Moretti, A. Moore, T. Moore, D. Gust, D. Prezzi, G. D. Scholes, E. Molinari, G. Cerullo, F. Troiani, C. A. Rozzi, M. Maiuri, *J. Phys. Chem. Lett.* **2024**, *15*, 4461.
[40] J. D. Schultz, J. L. Yuly, E. A. Arsenault, K. Parker, S. N. Chowdhury, R. Dani, S. Kundu, H. Nuomin, Z. Zhang, J. Valdiviezo, P. Zhang, K. Orcutt, S. J. Jang, G. R. Fleming, N. Makri, J. P. Ogilvie, M. J. Therien, M. R. Wasielewski, D. N. Beratan, *Chem. Rev.* **2024**, *124*, 11641.
[41] R. Muñoz-Mármol, S. Raj, M. Russo, G. Serra, H. Zhao, G. Bassi, A. Lucotti, F. Scotognella, G. Cerullo, G. Lanzani, M. Tommasini, M. Maiuri, A. Narita, G. M. Paternò, *Small Methods* **2025**, 2500419.
[42] D. Zigmantas, T. Polívka, P. Persson, V. Sundström, *Chemical Physics Reviews* **2022**, *3*, 041303.
[43] S. Jana, S. Prasad, H. L. Nguyen, D. V. Le, H.-S. Tan, *J. Chem. Phys.* **2025**, *162*, 164311.
[44] D. Timmer, M. Gittinger, T. Quenzel, A. R. Cadore, B. L. T. Rosa, W. Li, G. Soavi, D. C. Lünemann, S. Stephan, M. Silies, T. Schulz, A. Steinhoff, F. Jahnke, G. Cerullo, A. C. Ferrari, A. De Sio, C. Lienau, *Nano Lett.* **2024**, *24*, 8117.
[45] L. T. Lloyd, R. E. Wood, F. Mujid, S. Sohoni, K. L. Ji, P.-C. Ting, J. S. Higgins, J. Park, G. S. Engel, *ACS Nano* **2021**, *15*, 10253.
[46] A. Lietard, C.-S. Hsieh, H. Rhee, M. Cho, *Nat. Commun.* **2018**, *9*, 891.
[47] W. R. Jeffries, K. Park, R. A. Vaia, K. L. Knappenberger Jr., *Nano Lett.* **2020**, *20*, 7722.
[48] F. Toffoletti, E. Collini, *J. Phys. Chem. Lett.* **2024**, *15*, 339.
[49] F. V. A. Camargo, Y. Ben-Shahar, T. Nagahara, Y. E. Panfil, M. Russo, U. Banin, G. Cerullo, *Nano Lett.* **2021**, *21*, 1461.
[50] D. Finkelstein-Shapiro, P.-A. Mante, S. Sarisozen, L. Wittenbecher, I. Minda, S. Balci, T. Pullerits, D. Zigmantas, *Chem* **2021**, *7*, 1092.
[51] F. Toffoletti, E. Collini, *Nanoscale Advances* **2025**, 1384.
[52] D. F. Swearer, H. Zhao, L. Zhou, C. Zhang, H. Robatjazi, J. M. P. Martirez, C. M. Krauter, S. Yazdi, M. J. McClain, E. Ringe, E. A. Carter, P. Nordlander, N. J. Halas, *Proc. Natl. Acad. Sci. USA* **2016**, *113*, 8916.
[53] D. Catone, L. Di Mario, F. Martelli, P. O'Keeffe, A. Paladini, J. Stefano Pelli Cresi, A. K. Sivan, L. Tian, F. Toschi, S. Turchini, *Nanotechnology* **2020**, *32*, 025703.
[54] S. Link, M. B. Mohamed, M. A. El-Sayed, *J. Phys. Chem. B* **1999**, *103*, 3073.
[55] R. Yu, L. M. Liz-Marzán, F. J. García de Abajo, *Chem. Soc. Rev.* **2017**, *46*, 6710.
[56] J. D. Hybl, A. Albrecht Ferro, D. M. Jonas, *J. Chem. Phys.* **2001**, *115*, 6606.
[57] M. Khalil, N. Demirdöven, A. Tokmakoff, *Phys. Rev. Lett.* **2003**, *90*, 047401.
[58] H. Baida, D. Mongin, D. Christofilos, G. Bachelier, A. Crut, P. Maioli, N. Del Fatti, F. Vallée, *Phys. Rev. Lett.* **2011**, *107*, 057402.
[59] M. G. Silva, D. C. Teles-Ferreira, L. Siman, C. R. Chaves, L. O. Ladeira, S. Longhi, G. Cerullo, C. Manzoni, A. M. de Paula, G. Della Valle, *Phys. Rev. B* **2018**, *98*, 115407.
[60] S. T. Roberts, J. J. Loparo, A. Tokmakoff, *J. Chem. Phys.* **2006**, *125*, 084502.
[61] F. Šanda, V. Perlík, C. N. Lincoln, J. Hauer, *The Journal of Physical Chemistry A* **2015**, *119*, 10893.
[62] M. Russo, K. E. McGhee, T. Virgili, D. G. Lidzey, G. Cerullo, M. Maiuri, *Molecules* **2022**, *27*, 7095.
[63] G. Della Valle, G. M. Conforti, S. Longhi, G. Cerullo, D. Brida, *Phys. Rev. B* **2012**, *86*, 155139.
[64] E. Carpene, *Phys. Rev. B* **2006**, *74*, 024301.
[65] R. Rosei, *Phys. Rev. B* **1974**, *10*, 474.
[66] M. Zavelani-Rossi, D. Polli, S. Kochtcheev, A.-L. Baudrion, J. Béal, V. Kumar, E. Molotokaite, M. Marangoni, S. Longhi, G. Cerullo, P.-M. Adam, G. Della Valle, *ACS Photonics* **2015**, *2*, 521.
[67] P. O'Keeffe, D. Catone, L. Di Mario, F. Toschi, M. Magnozzi, F. Bisio, A. Alabastri, R. Proietti Zaccaria, A. Toma, G. Della Valle, A. Paladini, *Laser Photonics Rev.* **2021**, *15*, 2100017.
[68] E. Lacroce, L. Bianchi, L. Polito, S. Korganbayev, A. Molinelli, A. Sacchetti, P. Saccomandi, F. Rossi, *Nanoscale Advances* **2023**, *5*, 6870.
[69] D. M. Jonas, *Annu. Rev. Phys. Chem.* **2003**, *54*, 425.
[70] J. Réhault, M. Maiuri, A. Oriana, G. Cerullo, *Rev. Sci. Instrum.* **2014**, *85*, 123107.
[71] L. P. DeFlores, R. A. Nicodemus, A. Tokmakoff, *Opt. Lett.* **2007**, *32*, 2966.
[72] S.-H. Shim, D. B. Strasfeld, Y. L. Ling, M. T. Zanni, *Proc. Natl. Acad. Sci. USA* **2007**, *104*, 14197.
[73] S.-H. Shim, M. T. Zanni, *Phys. Chem. Chem. Phys.* **2009**, *11*, 748.
[74] D. Brida, C. Manzoni, G. Cerullo, *Opt. Lett.* **2012**, *37*, 3027.
[75] P. G. Etchegoin, E. C. Le Ru, M. Meyer, *J. Chem. Phys.* **2006**, *125*, 164705.
[76] P. B. Johnson, R. W. Christy, *Phys. Rev. B* **1972**, *6*, 4370.
[77] R. H. M. Groeneveld, R. Sprik, A. Lagendijk, *Phys. Rev. B* **1995**, *51*, 11433.
[78] Z. Lin, L. V. Zhigilei, V. Celli, *Phys. Rev. B* **2008**, *77*, 075133.
[79] J. B. Smith, H. Ehrenreich, *Phys. Rev. B* **1982**, *25*, 923.
[80] O. A. Yeshchenko, I. S. Bondarchuk, V. S. Gurin, I. M. Dmitruk, A. V. Kotko, *Surf. Sci.* **2013**, *608*, 275.